CSIRO PUBLISHING

International Journal of Wildland Fire **2015**, *24*, 461–469
http://dx.doi.org/10.1071/WF14036

Estimating radiated flux density from wildland fires using the raw output of limited bandpass detectors

Robert L. Kremens[A,C] *and Matthew B. Dickinson*[B]

[A]Rochester Institute of Technology, Chester F. Carlson Center for Imaging Science, 54 Lomb Memorial Drive, Rochester, NY 14623, USA.
[B]USDA Forest Service, Northern Research Station, 359 Main Road, Delaware, OH 43015, USA.
[C]Corresponding author. Email: kremens@cis.rit.edu

Abstract. We have simulated the radiant emission spectra from wildland fires such as would be observed at a scale encompassing the pre-frontal fuel bed, the flaming front and the zone of post-frontal combustion and cooling. For these simulations, we developed a 'mixed-pixel' model where the fire infrared spectrum is estimated as the linear superposition of spectra of many ($n \sim 30$) greybody emitters of randomly selected areal fraction, emissivity and temperature. Our model neglects contributions from atomic and molecular line emission from combustion gasses. The purpose of these simulations was to allow unambiguous use of limited bandwidth detectors to estimate the total power emitted from a wildland fire. From the simulations we observed a well-defined relationship between ground-leaving radiance (W m^{-2} sr^{-1}) and limited bandpass sensor-reaching radiance for many different detector spectral responses. Error in the relationship is least when the detector sampled in the mid-wave portion of the infrared spectrum (~3–5 μm) where flaming combustion emits most strongly. We validate our approach to estimating total power using data from experimental burns. The ability to estimate total power from limited bandpass measurements has great utility in the observation of wildland fires from ground-based instruments and aircraft and satellite platforms.

Additional keywords: infrared detection, radiated energy.

Received 19 March 2014, accepted 6 December 2014, published online 27 February 2015

Introduction

In most areas of remote sensing, the emission, transmission and reflection characteristics of the target are well known through laboratory or field measurements or, ideally, a combination of the two. Emission, transmission and reflection are often known as a function of wavelength, which allows wavelength-specific methods to be used to identify and quantify remotely sensed targets. By contrast, in remote observation of wildland fires, very few measurements have been made of the emission spectra, emissivity, angular distribution or any other physical parameters of interest to remote sensing observers, despite the fact that wildland fires have been observed from airborne and satellite remote sensing platforms for decades (see review in Kremens *et al.* 2010). Further confounding fire observations is the fact that most observed fire ground sample areas, even at high resolution, are 'mixed pixels', a combination of flames and non-flaming background of a range of temperatures.

A remote sensing detector is sensitive to radiation in a spectral passband that is defined by the detector spectral response, transmission of the various optical elements, and transmission of the atmosphere that intervenes between the ground and the atmosphere. The governing equation for detection is:

$$S = \int R(\lambda)T_a(\lambda)T_o(\lambda)M(\lambda)Gd\lambda \qquad (1)$$

where S is the signal generated by a detector, $R(\lambda)$ is the spectral responsivity of the detector, $T_a(\lambda)$ is the atmospheric transmission from the source to the detector, $T_o(\lambda)$ is the transmission of the optics in the system, $M(\lambda)$ is the spectral radiance of the source, G is a factor relating lens area and other geometric factors to the received signal, and the integral is over all wavelengths. When a well-characterised detector of limited bandwidth is used to observe a 'mixed fire pixel' as defined above without any other information, it is impossible to know the total surface-leaving power density of the target from the received signal alone because of the dependence on the spectral characteristics of the source and the effects of the intervening atmosphere. If the goal of remote sensing observations of wildland fire is to know not only the position of the fire but the emissive power and energy density, then we require additional information about the spectra, areal fractions of the mixed components and other radiative properties (emissivity, reflectivity and transmission). This additional information may be obtained by using more than one spectral band (e.g. Riggan *et al.* 2004; Daniels 2007; Kremens *et al.* 2010).

An example of the preceding problem is shown in Fig. 1. In this example, two blackbodies emit radiation according to the Boltzmann radiation law. One source (e.g. a flame) has a temperature of 1300 K and an emissivity of 0.09. The other source has a temperature of 500 K and an emissivity of 0.8.

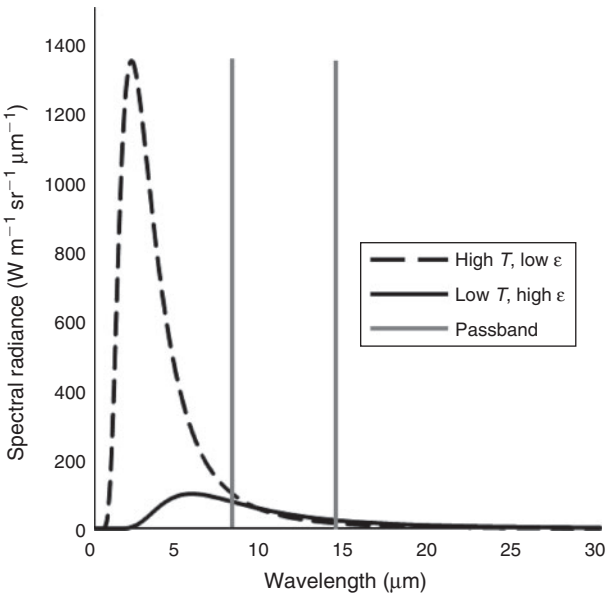

Fig. 1. Radiation as observed in a limited spectral bandwidth from two sources of different temperatures (T) and emissivity (ε). The total radiance emitted from the high0temperature source (dashed line, 1300 K) is ~five times larger than the radiance from the low-temperature source (500 K), even though the radiance observed in a typical 'long-wave infrared' (8–14 μm) detector is the same.

These examples represent a fire of small flame length and the warm background after the passage of the fire. The power received by a detector with a bandwidth of 8–14 μm for both spectra is the same, even though the hot source has more than five times as much total power output as the cooler source. Using a detector with limited bandwidth and no other information about the spectral signature of the source, we cannot uniquely determine the total power emitted by the source.

The radiation from a fire originates from several sources: blackbody emission from incandescent soot within the flame envelope; fuels undergoing pyrolysis and glowing combustion; hot ground in and behind the flame front; large woody fuels burning behind the flame front; and potentially strong band emission from hot water vapour (Frankman *et al.* 2008), unburned hydrocarbons (CO, H_2O, CO_2) and other gaseous components produced during the combustion process. The emissions from CO_2 and water vapour are strongly absorbed by the intervening atmosphere, leaving the blackbody radiation from the fire in the long-wave infrared (LWIR) and other high-transmission regions as the primary observable radiation for a distant observer (Schott 1997: p. 84). Atmospheric transmission is well understood (Schott 1997: pp. 74–85), at least where smoke is not dense, and for the purposes of this paper we assume that atmospheric effects on the spectral characteristics of the radiation that reaches the detector can be quantified using atmospheric transmission models such as MODTRAN. Our primary goal for this work, therefore, is to simulate a wildland fire ground sample area as would be seen by a remote sensing detector, and to derive spectral properties for this area that will allow unique determination of the emitted flux density using a detector of limited spectral bandwidth.

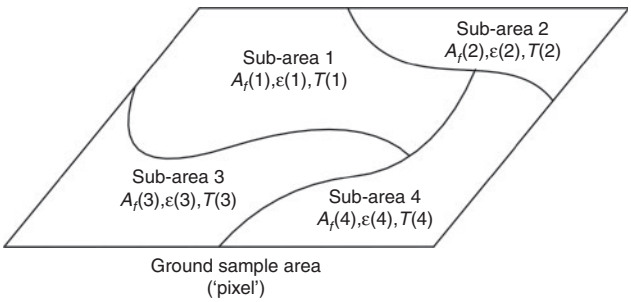

Fig. 2. Schematic representation of the simulation process showing in this case $n = 4$ different emitting components in the ground sample area. For our simulations, we used between 2 and 30 different sub-components of the ground sample area to simulate fire scenes of varying complexity, and to determine if there were any effects of sub-area complexity on the fit temperature or quality of fit using a single-temperature distribution.

Methods

Simulating total and limited bandpass radiation from mixed-temperature fire pixels

We formulated a computer simulation model using the Python language and various adjunct Python libraries (SciPy, matPlotlib, Numpy and csv). The model developed for these simulations uses the following assumptions:

1. A fire ground sample area consists of multiple emitting surfaces or volumes, each with an independently assigned temperature, emissivity and fractional area (Fig. 2). We report results from 30 fractional areas because from our studies, the relationships between number of fractional areas and average temperature, emissivity, power and other factors asymptote at that number of sub-areas. The maximum temperature of a wildland fire flame is ~1300 K (Butler *et al.* 2004), though somewhat different values are obtained depending on the measurement method and its spatial and temporal scale (e.g. Martin *et al.* 1969; Sullivan *et al.* 2003). The minimum temperature we consider for these simulations is 300 K, representative of unburned background. Each of the areas in the simulation is independent and has a random temperature assigned to it (using a uniform probability distribution over the range of 300–1300 K sub-area temperature).
2. The emissivity of a flame can vary from 0.05 (thin flames in the direction of observation) to values approaching 1 (for ≥4-m flame depth, e.g. Johnston *et al.* 2014). The emissivity of fuels undergoing pyrolysis and the warm soil background can vary between 0.6 and 0.85 (Kremens *et al.* 2003). We know of no measurements of the emissivity of spreading flames from a nadir perspective and limit emissivity to 0.85, which would be representative of a thick flame and its hot background. Each of the 30 areas in the simulation has an independent emissivity assigned to it, the lower temperature areas (<600 K) having emissivity biased towards higher values (0.6–0.85) as these low temperatures represent warm background.
3. The spectral flux density and spectral power density from a 'mixed' ground sample area may be obtained by superposition of the spectral emissions from the multiple emitting surfaces.

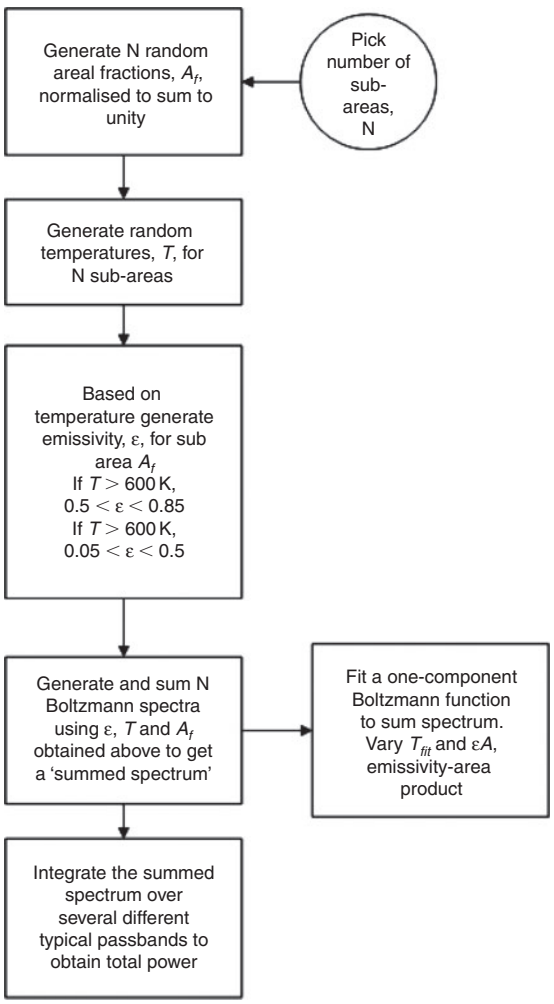

Fig. 3. Flow chart showing the major steps in the simulation whose results are used in combination with raw detector output from limited bandpass detectors to estimate total fire-radiated power.

4. The radiation from the ground sample area or volume is distributed uniformly in space ('Lambertian radiator' assumption, that is, the radiant intensity varies as $I_0 \cos\phi$, where I_0 is the intensity normal to the emitting surface or volume and ϕ is the angle from the normal to the surface to the direction of interest).

Our simulation method is similar to one conducted earlier by Wooster *et al.* (2003) but here we extend the utility of the model to include any detector spectral response and all possible sets of fire–background conditions. In each simulation of a fire pixel (Fig. 3), we generated a spectrum by summation of 30 blackbody spectra, each with a randomly selected emissivity (subject to the constraints in number 2, above, see Àgueda *et al.* 2010), randomly selected temperature (subject to the constraints in 1, above) and randomly selected areal fractions (where the areal fractions sum to 1, the total area in the field of view of the detector). We repeated this process 10 000 times to represent an ensemble of possible areal fractions, temperatures and emissivity from the ground sample area. From previous manual calculations, we believed that the summation obtained by the above process would be very nearly identical in spectral form to a Boltzmann spectral distribution from a single-temperature source. Because of the highly nonlinear monotonic functional dependence (T^4) of the total blackbody emissive power on the temperature, we hypothesised that the overall spectral shape from such a summation should be dominated by the highest temperature (flaming) components. To test this hypothesis, we fit a Boltzmann distribution with a *single* temperature to the summed spectra using a nonlinear curve fit method. We examined the goodness of fit of this single-temperature distribution using conventional metrics and also compared the power and energy densities from numerical integration of both the fit and data from the multi-object simulation. The fit parameters are the temperature (which controls the width and peak location of the distribution) and the emissivity-fractional area product (which controls the 'height' of the distribution, see Kremens *et al.* 2010).

In addition to calculating these simulated spectra, we computed the received detector power for eight different limited bandwidth detector systems as defined in Table 1. These systems have responses that are typical of commercially available single- and multiple-detector arrays that would be used for observation of wildland fire. Note that the 'WASP' detector in Table 1 corresponds to the airborne sensor system designed and built at the Rochester Institute of Technology for observation of wildland fires. This system has been deployed ~30 times to create time-sequenced observations of wild and prescribed fires (Ononye *et al.* 2005; Dickinson *et al.* 2014). Tower-deployed sensors used in Kremens *et al.* (2012) and Dickinson *et al.* (2014) are also simulated. With results of the simulations, we parameterise a statistical model by relating total radiant exitance to sensor-reaching radiance. Standard laboratory calibration procedures are then used to relate sensor-reaching power density to raw response of a limited passband detector (digital number, DN; Palmer and Grant 2010; Fig. 4). Thus, we demonstrate how a measurement of only the digital signal from a limited bandwidth detector can be used to derive a direct measure of ground-leaving power flux density.

An ideal detector has a flat response across all wavelengths within its passband. However, detectors approach this ideal to different degrees and, thus, we include spectral response in Eqn 1. We incorporate spectral response in calculated received detector power for a sample of detectors (Tables 1 and 2) for which spectral response meets the ideal to varying degrees (e.g. Fig. 5). For all but one of the sensors we have experimentally measured spectral response data and, for those sensors, the Planck function is multiplied by wavelength-specific window transmission which ranges from zero outside of the passband (transmission is zero) to values that fluctuate above zero within the passband (see Fig. 5). The KBr window sensor has a nearly flat spectral response function within the passband and, for that sensor, average transmission is used.

Validating estimates of total fire radiation

As a limited validation of our simulations, we compare their results with estimates of fire radiation from dual-band radiometry (see Kremens *et al.* 2010 for background on dual-band radiometry). Mid-wave infrared (MWIR) and LWIR sensors

Table 1. Specifications for infrared cameras and single-pixel sensors for which we simulated detector irradiance

Spectrum name refers to the spectral response function. The detectors represent the bulk of commercially available detector systems (imaging and point detectors). The CaF_2, LWPSi, KBr and Sapphire detector spectral characteristics represent commonly used windows for thermopile detectors. The KBr sensor was simulated with a flat spectral response that is close to the spectral transmission of the KBr window. Transmission (T) is proportional energy transmission through the sensor window in the waveband to which the sensor responds. Citation indicates study in which the sensors were used (see footnote). For ease of comparison, the table is sorted by the root mean squared error of the relationship between total and limited passband response to simulated fire pixels (see Table 2)

Sensor name	Transmission	Citation	Manufacturer	Material	Detector	Spectrum name
KBr	0.92	–	Dexter Research	KBr	Various	NA
CaF_2	0.60	1,2	Dexter Research	CaF_2	DR 2M CaF_2	DC-6100 – U8
Sapphire	0.85	3	Dexter Research	Sapphire	ST60 DX-1001	DC-6216-U1
MW	0.60	2	Dexter Research	CaF_2	ST60 DX-0852	DC-6100-U8
LWPSiL1	0.70	1,2	Excelitas	Silicon	PE TPS334	DC-6188-L1
LW WASP	0.95	2	Phoenix	Ge AR (lens)	QWIP	On file
LWPSiL2	0.70	2	Dexter Research	Silicon	ST60 DX-0852	DC-6186-L2
LWPSiW1	0.83	3	Dexter Research	Silicon	ST60 DX-1001	DC-6073-W1

[1]Kremens *et al.* 2012; use CaF_2 and LWPSiL1 in dual-band combination on towers; [2]Dickinson *et al.* 2014; use MW and LWPSiL2 in dual-band combination on towers and, secondarily, CaF_2 and LWPSiL1 in combination as above; [3]Studies in progress use Sapphire and LWPSiW1 in dual-band combination on towers.

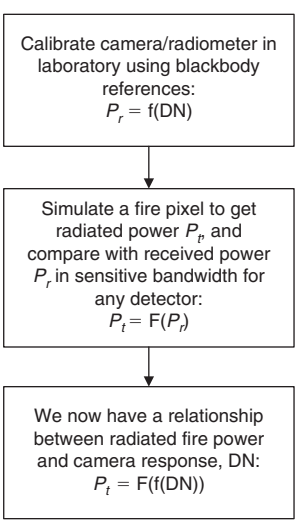

Fig. 4. The process for using simulations outlined in Fig. 3 and laboratory calibration measurements to estimate total radiated power from wildland fires using output from a limited bandwidth detector. P_r = power received by the detector in its sensitive passband, P_t is the total power radiated by the fire and DN is the raw digital count from the sensor (pre-corrected for offset and nonlinearities, if necessary).

were positioned over small plot (8 × 8 m) fires in mixed oak litter and woody debris (for details, see Bova and Dickinson 2008 and Kremens *et al.* 2012). Specifications and detector-reaching power for the sensors used in these experiments are summarised in Tables 1 and 2. We compare peak ground-leaving fire-radiated flux density (FRFD, W m^{-2}) and total fire-radiated energy density (FRED, MJ m^{-2}) estimated from dual-band radiometry with estimates of the same quantities derived from our simulation results and the raw output of limited passband sensors.

Nadir-viewing, side-by-side MWIR and LWIR sensors were placed 3.9 m above the ground and the voltage output was logged at 10-s intervals. The LWIR (hereafter LWPSi-L1, Tables 1 and 2) and MWIR (hereafter CaF_2, Tables 1 and 2) detectors have a linear response to the power that reaches the detector through the sensor window (detector-reaching power). It is the window composition and coatings that determine passband and wavelength-specific (spectral) transmission. Spectral response (a function of both transmission and detector response) data were obtained from Dexter Research Inc., Dexter, MI, USA, (for the CaF_2 window sensor) and Excelitas Technologies Corp., Waltham, MA, USA, (for the LWPSi-L1 window sensor) and are shown in Fig. 5. The relationship between detector voltage output (DN) and blackbody excitance was determined using the near-extended source approach wherein the blackbody is larger than the field of view of the sensor (Palmer and Grant 2010). Total excitance (leaving the blackbody, kW m^{-2}) and excitance within the passband of the sensor were calculated by integrating the Planck equation (after accounting for sensor spectral response) over all wavelengths for each blackbody temperature:

$$L_T = \int_0^\infty 2hc^2\lambda^{-5}\left(e^{\frac{hc}{\lambda kT}} - 1\right)^{-1} d\lambda \quad (2)$$

$$L_{band} = \int_0^\infty 2hc^2\tau(\lambda)\lambda^{-5}\left(e^{\frac{hc}{\lambda kT}} - 1\right)^{-1} d\lambda \quad (3)$$

where h is Planck's constant, c is the speed of light, λ is the wavelength, T is the temperature for which the flux is calculated and $\tau(\lambda)$ is the normalised bandpass response function for the detector.

Detector-reaching radiance (W m^{-2} sr^{-1}) is calculated from excitance through division by π (Palmer and Grant 2010).

Table 2. Nonlinear regression parameters and fit between total radiance (L_T, W m^{-2} sr^{-1}) and radiance reaching a range of detectors through a sensor window

Power cut-off points (50%) roughly describe spectral response, though measured spectral response is used in simulations. No correction for atmospheric absorption is included in these relationships, which would be necessary for applying to airborne and satellite-borne sensors (Dickinson *et al.* 2014). All results are based on 10 000 fire pixels for which 30 sub-pixel aerial fractions and their temperature and emissivity are chosen at random within constraints (see text and Table 3). Mean, minimum and maximum sensor-reaching radiance (W m^{-2} sr^{-1}) from simulations are shown for each limited bandpass sensor. Nonlinear regression parameters relate total ground-leaving radiance to a power of sensor-reaching radiance (e.g. Eqns 6 and 7). The table is sorted by the root mean squared error (RMSE) of total predicted radiance. RMSE is also shown as a proportion of mean total radiance. Further summaries of the simulations are reported in Table 3

	Cut off (μm)		Radiance (W m^{-2} sr^{-1})			Power fit			
Detector	Lower	Upper	Mean	Min	Max	*b*	*M*	RMSE (W m^{-2} sr^{-1})	RMSE (proportion)
KBr	0.15	30.00	3683	1047	8397	1.0870	1.0000	1×10^{-6}	1×10^{-10}
CaF_2	0.15	12.50	3557	957	8252	1.4130	0.9723	14.2	0.004
Sapphire	0.10	6.50	2679	604	6501	3.0868	0.9085	54.7	0.01
MW	3.00	5.00	1339	364	2984	3.0828	0.9958	71.8	0.02
LWPSiL1	5.50	20.00	1060	448	1967	0.4728	1.2972	245.8	0.06
WASP	8.00	9.20	189	85	341	3.2823	1.3535	286.8	0.07
LWPSiL2	6.50	20.00	608	285	1068	0.4601	1.4138	306.5	0.08
LWPSiW1	8.00	14.00	350	169	603	0.7710	1.4590	331.1	0.08

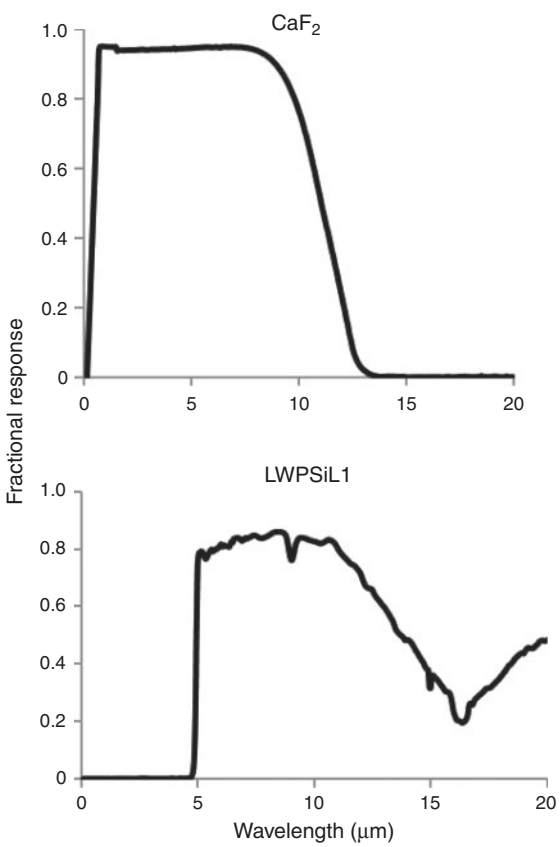

Fig. 5. Spectral response for a mid-wave and long-wave infrared sensor. The top figure shows transmission for a calcium fluoride window (the 'U8' transmission spectrum) measured by Dexter Research. The bottom figure shows the transmission spectrum for a germanium window (the 'L1' spectrum). See Tables 1 and 2 for more details.

Sensor-reaching radiance is expressed as follows respectively for the LWPSi-L1 and CaF_2 window sensor:

$$L_{LW} = \frac{7.70DN + 277.38}{\pi} \quad (4)$$

$$L_{MW} = \frac{7.56DN + 127.38}{\pi} \quad (5)$$

where *DN* is the digital number from the analogue-to-digital converter in the detector system. Using detector-reaching radiance instead of detector irradiance (analogous to excitance, W m^{-2}) allows us to ignore sensor height under the assumption that as the field of view of the sensor increases, power flux density per unit solid angle remains constant. This assumption has not been tested for sub-pixel flames in wildland fires. Having obtained the sensor-reaching irradiance from Eqns 4 and 5 above and the *DN* from the digitised output of the detectors, we use the results of our simulations (that relate sensor-reaching radiance to ground-leaving fire radiance) and the assumption of Lambertian radiation from the fire to obtain FRFD. Time integration of FRFD yields FRED.

Results

Graphical examples of the single-temperature fit applied to the sum spectra are shown in Fig. 6, and mean and range of the pixel temperature and emissivity-fractional area (εA) product of the blackbody (Boltzmann) spectra that best fit simulated pixels (along with the range in pixel aerial fractions and their temperatures and emissivities) are given in Table 3. The εA product emerges from the calculation of FRFD from dual-band data (Kremens *et al.* 2010) and is reported here for convenience. Total power of the summed spectra was closely related to power derived from the best-fit blackbody pixel temperature (total power = 448 + 0.999 × blackbody power; root mean square error (RMSE) = 103 W m^{-2}). The power law fit between total

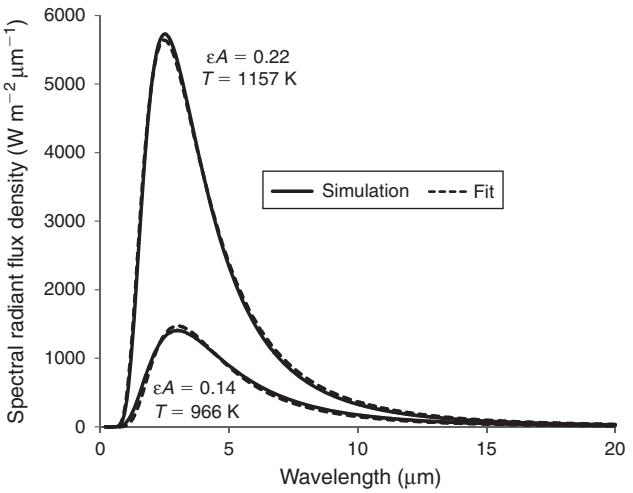

Fig. 6. Graphical examples of the curve fit to simulated data using a single-temperature Boltzmann distribution. We show representative examples for pixels with six sub-areas within the ground sample area (see Fig. 2). We varied the temperature (T) and emissivity area product (εA) in this two-parameter nonlinear fit to simulation results. Summed spectra yielded 22.1 kW m^{-2} (upper curves) and 6.9 kW m^{-2} (lower curves) representing a case with significant flaming combustion within a pixel, and a case where there is more hot background and less flaming combustion.

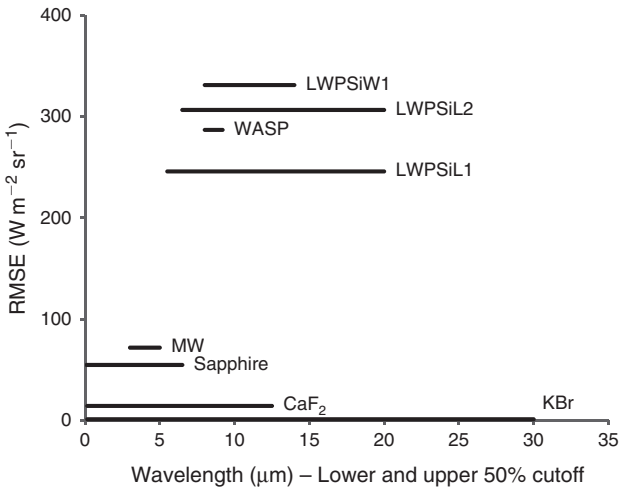

Fig. 7. Root mean square error (RMSE) for predicted radiance (W m^{-2} sr^{-1}) for simulations of the mid-wave and long-wave portions of the electromagnetic spectrum and a series of common detectors (Table 2). Radiance RMSE is from simulations with 30 fractional areas. Atmospheric absorption is not included in these simulations.

Table 3. Summary output derived from the simulations

Total radiance is derived from summed power over each ground sampling area (i.e. pixel) obtained by summation of the blackbody spectral emissions from all ($n = 30$) aerial fractions (see Figs 2–4). A nonlinear curve fit procedure was used to determine the pixel temperature and emissivity area product that best reproduced the summed spectra (e.g. Fig. 6). The mean, minimum and maximum aerial fractions and emissivity and temperatures of those aerial fractions across all 10 000 simulations are also shown

Variable	Mean	Minimum	Maximum
Total radiance (W m^{-2} sr^{-1})	4003	1139	9127
Fit temperature (K)	1080	763	1230
Fit emissivity area product (dimensionless)	0.16	0.06	0.27
Aerial fractions (proportion of unity)	0.03	6×10^{-8}	0.10
Emissivity of sub-pixel areas (dimensionless)	0.39	0.05	0.85
Temperature of sub-pixel areas (K)	800	300	1300

radiance and radiance within a limited passband is described in Table 2. The greatest RMSE was for detectors whose passband was limited to the long-wave portion of the infrared spectrum and thereby received a smaller fraction of total power (Fig. 7 and Table 2). As an example, in Fig. 8, the WASP long-wave detector exhibits greater error (i.e. scatter around a fitted regression trend) than the wide-band KBr detector. Regardless of relative differences among sensors, RMSE as a fraction of the mean of total power was $<10\%$ for all sensors (Table 2).

We evaluated the validity of the simulations by using simulation results to predict ground-leaving FRFD and FRED from the raw output of LWPSiL1 and CaF_2 limited passband

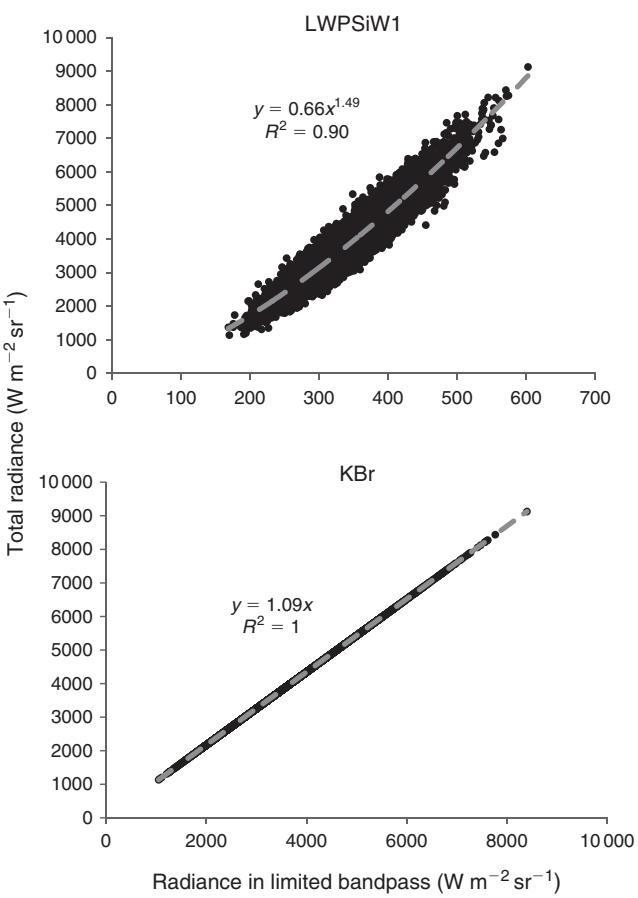

Fig. 8. Example relationships between ground-leaving total radiance and radiance in the passband of the detector for a long-wave (LWPSiW1) and wide passband detector (KBr). See Tables 1 and 2 for detector characteristics. The points in the graphs come from the simulation.

Table 4. Average slopes relating ground-leaving fire-radiated flux density (FRFD, W m^{-2}) measured by dual-band radiometry (e.g. Kremens *et al.* 2010) and FRFD estimated from measurements from two limited bandpass sensors and Eqns 9 and 10

Shown are the average slopes and their 95% confidence intervals estimated from least-squares regression through the origin. Data are from $n = 8$ replicate burns from the 8 × 8-m plot burn experiment described in Bova and Dickinson (2008) and Kremens *et al.* (2012). Slopes would be unity with perfect agreement between the methods of estimating FRFD. There was no co-variation in these slopes with either peak FRFD or fire-radiated energy density (FRED, MJ m^{-2}) across the range in fuel consumption and surface fire behaviour obtained in these experiments (Table 5). Example slope calculations from a single replicate of the burn experiment are shown in Fig. 9

Dependent variable	Independent variable	Average slope (+/− 95% CI)
Dual-band FRFD	LWPSiL1 FRFD	1.07 (+/−0.16)
Dual-band FRFD	CaF_2 FRFD	1.16 (+/−0.02)

sensors and by comparing those FRFD and FRED estimates with those derived from dual-band radiometry. Total ground-leaving and limited passband radiance are calculated from simulation results. Then, total ground-leaving radiance is related to limited passband radiance at the detector by nonlinear regression. The regression parameters were estimated separately for LWPSi-L1 and CaF_2 sensors as follows:

$$L_T = b(L_{LW})^M \quad (6)$$

$$L_T = b(L_{MW})^M \quad (7)$$

where L_T is total ground-leaving radiance (W m^{-2} sr^{-1}) and b and M are the parameters. The exponential model with an intercept of zero was chosen over a linear regression on both untransformed and log-transformed data because they showed large errors in recovering near-background radiative flux densities. Ground-leaving FRFD is then calculated from radiance

$$\text{FRFD} = L_T \pi \quad (8)$$

The final equations for ground-leaving FRFD incorporate parameters in Table 2 and combine Eqns 4 and 6 for LWPSiL1:

$$\text{FRFD} = \left(0.473\left(\frac{10.147DN - 85.085}{\pi}\right)^{1.297}\right)\pi \quad (9)$$

and Eqns 5 and 7 for CaF_2 sensors:

$$\text{FRFD} = \left(1.413\left(\frac{7.212DN - 4.758}{\pi}\right)^{0.972}\right)\pi \quad (10)$$

No-intercept, linear regression slopes between FRFD estimated from dual-band radiometry and FRFD estimated from the raw output of limited bandpass detectors and Eqns 9 and 10 approach unity (Table 4 and Fig. 9). The small plot experiments

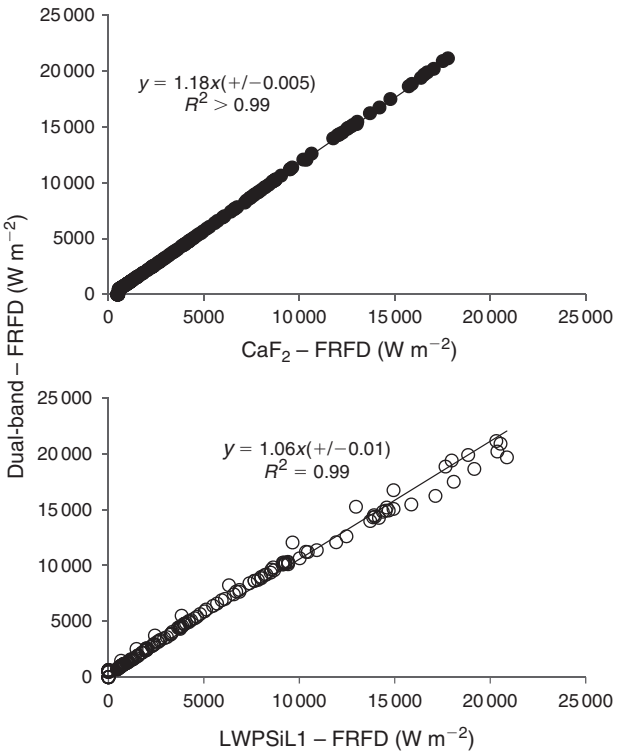

Fig. 9. Example relationship between ground-leaving fire-radiated flux density (FRFD, W m^{-2}) measured from dual-band radiometry and FRFD estimated from measurements from limited bandpass sensors and Eqns 9 and 10 for the CaF_2 and LWPSiL1 sensors (see overall results in Table 4). The same sensors are used for both dual-band and limited passband estimates. Data are from the replicate burn with the highest peak FRFD among $n = 8$ replicate experiments described in Bova and Dickinson (2008) and Kremens *et al.* (2012). The slopes from this and the other replicates were used to test for bias between estimates derived from single-bandpass data and dual-band radiometry (Table 4 and Fig. 10).

Table 5. Mean and ranges of peak fire-radiated flux density (FRFD) and fire-radiated energy density (FRED) measured from dual-band radiometry for $n = 8$ replicate burns from the 8 × 8-m plot burn experiment described in Bova and Dickinson (2008) and Kremens *et al.* (2012)

Fuel consumption is calculated on an ash- and moisture-free basis. Results from these experiments are also shown in Table 4 and Figs 9 and 10

	Mean	Minimum	Maximum
Fuel consumption (kg m^{-2})	1.1	0.15	3.25
Peak FRFD (W m^{-2})	14 062	3760	21 157
FRED (MJ m^{-2})	4.73	0.38	10.10

spanned a wide range in fuel consumption, peak FRFD and FRED (Table 5). For neither sensor did slopes co-vary with peak FRFD or FRED estimated from dual-band radiometry. Slopes of the linear regressions between peak FRFD and FRED estimated from dual-band radiometry and the same quantities estimated from CaF_2 and LWPSiL1 detector output and simulation results also approached unity (Fig. 10).

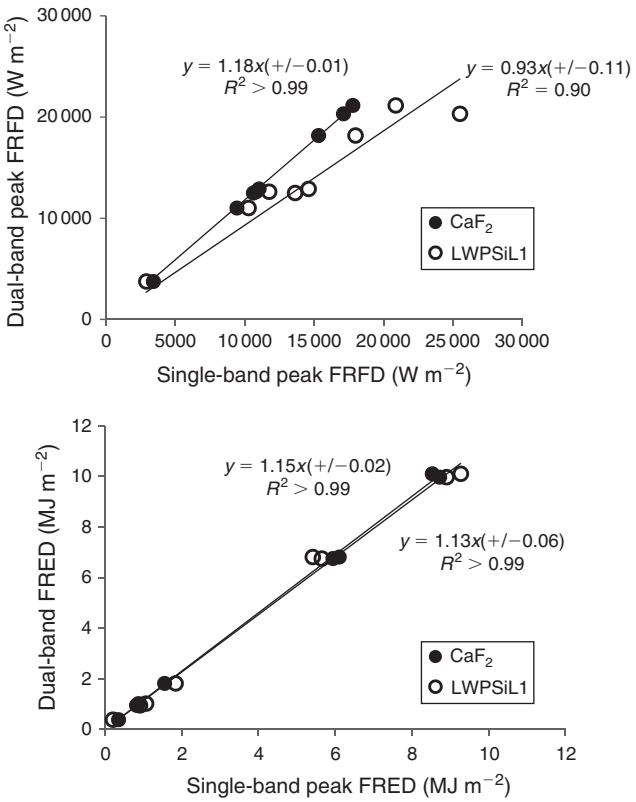

Fig. 10. Relationships between peak fire-radiated flux density (FRFD, top) and fire-radiated energy density (FRED, bottom) measured from dual-band radiometry and the same quantities estimated from single-band LWPSiL1 and CaF_2 sensor measurements and simulation results. Sensor characteristics are provided in Tables 1 and 2. Slopes and their 95% confidence intervals (in parentheses) are shown. With perfect agreement between dual-band and limited passband methods, slopes would be unity. Results are from $n = 8$ replicate burns from the 8×8-m plot burn experiment described in Bova and Dickinson (2008) and Kremens *et al.* (2012).

Discussion

The primary motivation for this work was to determine if we could estimate, with reasonable error, the ground-leaving radiant flux density from a wildland fire given only measurements in a limited bandwidth. Using our simulations, we have derived relationships between the signal from common limited bandwidth detectors and ground-leaving radiant power from a fire. Our results will be useful for future observations and also for designing airborne fire observation sensors. Our simulations (Fig. 8 and Table 2) suggest that total power will be an exponential function of detected power across a range of detectors that, unlike the KBr detector, sample a limited part of the infrared spectrum. The close relationship between total power calculated directly from the summed spectra and blackbody power (estimated from the blackbody temperature that best describes the summed spectra from each mixed-temperature pixel) reflects dominance of pixel radiation by active combustion. This relationship provides a potential means of using fire model output to simulate remotely sensed wildland fire scenes.

Error arising from the relationship between total emissive power and sensor-reaching power in a limited passband is highest where the detector passband does not include the mid-wave (~3–5 μm) or includes only a part of the mid-wave (Fig. 7, Table 2). Error increases where mid-wave radiation is not sensed because the majority of emissive power from fires comes from flames whose emissions peak in the mid-wave (e.g. Johnston *et al.* 2014). Our simulations and Fig. 1 suggest that if a detector is not sensitive to the mid-wave region of the spectrum the same emissive power can arise from a range of combinations of temperature, emissivity and fractional area within a mixed-temperature fire pixel. Passband width has a less consistent effect on error with the exception of the KBr detector whose passband (0.1–30 μm) encompasses most of infrared radiation from fires and exhibits the least error (Fig. 7).

Referring now to Fig. 8, we can begin to understand the nature of the relationship between the total energy radiated by a fire and the energy received by a limited bandwidth detector. The very wide bandwidth 'KBr' detector (with nearly flat lens transmission) receives power from the fire at virtually all wavelengths of importance, so the relationship between radiated power and detected power is unique and linear. The KBr system is insensitive to the temperature of the source. It should be noted that a detector of this bandwidth is not realisable in practice because the atmosphere is opaque to many wavelengths at long standoff distances (hundreds of metres) from the fire (Palmer and Grant 2010). The response of a limited bandwidth detector, however, depends on the source's apparent temperature. The error in surface-leaving radiance associated with the LWPSiW1 sensor in Fig. 8 is related to effective temperature distribution in our simulations. The error is least at high and low flux densities because there are fewer ways to create these extremes of flux density. Intermediate levels of radiated flux density can be created in many ways using various combinations of temperature, emissivity and fractional pixel area; hence the breadth of the error distribution.

In a limited validation exercise, we show that our simulation results can be used to derive relatively accurate estimates of FRFD (Table 4, Fig. 9), peak FRFD and FRED (Fig. 10). We demonstrate this for oak litter fuels with added woody material covering a wide range in fuel consumption. It should be noted that in evaluating our simulation approach, we compare estimates of FRFD, peak FRFD and FRED derived from simulation results and measurements from limited bandpass long-wave (LWPSiL1) and mid-wave (CaF_2) sensors to estimates from dual-band radiometry that employ data from the same sensors in combination (Kremens *et al.* 2010). Estimates based on data from the CaF_2 sensor exhibited higher precision but lower accuracy than data from the LWPSiL1 sensor and tended to underestimate the result from dual-band radiometry. Less precision for the LWPSiL1 sensor would be expected because the sensor has limited sensitivity to the mid-wave region of the infrared spectrum. Regardless, linear regression slopes of dual-band *v.* single-band estimates were close to unity for both sensors, ranging from 0.93 to 1.18. Comparison of estimates from independent sets of instruments would be a stronger test of the approach. Also, more extensive validation should be carried out involving other fuels, more intense fires, and other instruments, particularly measurements from aircraft. Dickinson *et al.* (2014) use our results to derive estimates of ground-leaving FRFD from airborne LWIR data after accounting for (spectral) atmospheric absorption of radiation.

For our simulations, we have defined a unique relationship between detected power and emitted power as shown by Eqns 9 and 10. In general we expect the form of Eqns 9 and 10 to remain the same regardless of the receiver spectral bandwidth. This very useful relationship means we can now estimate the total radiative power produced by a fire using measurements from limited bandpass instruments without resorting to in-fire (ground) calibration instruments or other guesses on apparent temperature, emissivity or fractional area of the fire. Future studies may examine various assumptions of our approach, including the particular peak flame temperature and emissivity values that we used, the extent to which hot gas emission violates the blackbody fire emission assumption, and the effects of violations in the Lambertian radiator assumption (e.g. Freeborn *et al.* 2008).

Conclusions

Using a numerical simulation, we have determined functional relationships between sensor-reaching flux density for limited bandpass sensors and surface-leaving flux density for mixed-temperature pixels characteristic of areas in and around wildland fire flaming fronts. Radiation detected by limited bandpass sensors relates closely to total ground-leaving radiation because power emanating from wildland fire pixels is dominated by high-temperature combustion. We believe these simulations to be general. By modelling a wide range of combinations of temperature, emissivity and sub-pixel fractional areas, these simulations represent a wide range of fire behaviour parameters. We do not restrict the areal fraction of the fire, and the simulations can be run easily with any sensor spectral sensitivity. Ignoring atmospheric interception of fire radiation, and confusion resulting from reflected and upwelled light in sensor spectral bands where solar radiation is present, error in total power estimated from these relationships will be least for sensors that are sensitive in the mid-wave infrared (~3–5 μm) region. The simulations also indicate that the inherent error in these estimates is at a minimum for both very low and very high sensor-reaching power, because there are fewer ways in which a fire 'scene' can produce these two extremes of radiation at the sensor. Our simulations suggest that error will be no greater than 10% of total power even for long-wave detectors. We provide a limited validation of the simulations from well-characterised surface fires in 8 × 8-m plots of mixed oak litter and woody fuels. Our approach demonstrates a method of deriving quantitative estimates of surface-leaving flux density using measurements from limited bandpass sensors, an advance we believe the wildland fire science community will find to be useful.

Acknowledgements

We thank Bret Butler and four anonymous reviewers for helpful feedback on the manuscript. This project was funded by the National Fire Plan and a grant from the Joint Fire Science Program (the RxCADRE project, 11–2-1–11).

References

Àgueda A, Pastor E, Perez Y, Planas E (2010) Experimental study of the emissivity of flames resulting from the combustion of forest fuels. *International Journal of Thermal Sciences* **49**, 543–554. doi:10.1016/J.IJTHERMALSCI.2009.09.006

Bova AS, Dickinson MB (2008) Beyond 'fire temperatures': calibrating thermocouple probes and modeling their response to surface fires in hardwood fuels. *Canadian Journal of Forest Research* **38**, 1008–1020. doi:10.1139/X07-204

Butler BW, Cohen J, Latham DJ, Schuette RD, Sopko P, Shannon KS (2004) Measurements of radiant emissive power and temperatures in crown fires. *Canadian Journal of Forest Research* **34**, 1577–1587. doi:10.1139/X04-060

Daniels A (2007) 'Field Guide to Infrared Systems'. (SPIE Publishing: Bellingham, WA)

Dickinson MB, Ellison L, Hudak A, Ichoku C, Kremens RL, Loudermilk L, O'Brien J, Paxton A, Schroeder W, Zajkowski T, Holley W, Hornsby B, Martinez O, Mauseri J, Peterson D (2014) Comparing ground, airborne, and satellite measurements of fire radiative power – developing methods and datasets for cross-scale validation. *International Journal of Wildland Fire*.

Frankman D, Webb BW, Butler BW (2008) Influence of absorption by environmental water vapor on radiation transfer in wildland fires. *Combustion Science and Technology* **180**, 509–518. doi:10.1080/00102200701741400

Freeborn PH, Wooster MJ, Hao WM, Ryan CA, Nordgren BL, Baker SP, Ichoku C (2008) Relationshiops between energy release, fuel mass loss, and trace gas and aerosol emissions during laboratory biomass fires. *Journal of Geophysical Research* **113**, D01301. doi:10.1029/2007JD008679

Johnston JM, Wooster MJ, Lynham TJ (2014) Experimental confirmation of the MWIR and LWIR grey body assumption for vegetation fire flame emissivity. *International Journal of Wildland Fire* **23**, 463–479. doi:10.1071/WF10143

Kremens R, Faulring J, Hardy C (2003) Measurement of the time–temperature and emissivity history of the burn scar for remote sensing applications. In '5th Symposium on Fire and Forest Meteorology and the 2nd International Wildland Fire Ecology and Fire Management Congress', 16–20 November 2003, Orlando, FL. Paper J1G.5. (American Meteorological Society: Boston, MA)

Kremens RL, Smith AM, Dickinson MB (2010) Fire metrology: current and future directions in physics-based measurements. *Fire Ecology* **6**, 13–25. doi:10.4996/FIREECOLOGY.0602013

Kremens RL, Dickinson MB, Bova AS (2012) Radiant flux density, energy density, and fuel consumption in mixed-oak forest surface fires. *International Journal of Wildland Fire* (In press). doi:10.1071/WF10143

Martin RE, Cushwa CT, Miller RL (1969) Fire as a physical factor in wildland management. In 'Proceedings Annual [9th] Tall Timbers Fire Ecology Conference'.10–11 April 1969, Tallahassee, FL. pp. 271–288. (Tall Timbers Research Station: Tallahassee, FL)

Ononye A, Vodacek A, Li Y, Wang Z (2005) Mapping of active fire area by image gradient technique using multi-spectral imagery. In 'Remote Sensing for Field Users. Proceedings of the 10th Biennial USDA Forest Service Remote Sensing Applications Conference', April 5–9 2004, Salt Lake City, UT'. [unpaginated] (American Society for Photogrammetry and Remote Sensing: Bethesda, MD) CD-ROM, ISBN 1–57083–075–4.

Palmer JM, Grant BG (2010) 'The Art of Radiometry'. (SPIE Press: Bellingham, WA)

Riggan PJ, Tissell RG, Lockwood RN, Brass JA, Pereira JAR, Miranda HS, Miranda AC, Campos T, Higgins R (2004) Remote measurement of energy and carbon flux from wildfires in Brazil. *Ecological Applications* **14**, 855–872. doi:10.1890/02-5162

Schott JR (1997) 'Remote Sensing, the Image Chain Approach'. (Oxford University Press: New York)

Sullivan AL, Ellis PF, Knight IK (2003) A review of radiant heat flux models used in bushfire applications. *International Journal of Wildland Fire* **12**, 101–110. doi:10.1071/WF02052

Wooster MJ, Zhukov B, Oertel D (2003) Fire radiative energy for quantitative study of biomass burning: derivation derived from the BIRD experimental satellite and comparison to MODIS fire products. *Remote Sensing of Environment* **86**, 83–107. doi:10.1016/S0034-4257(03)00070-1